Study of the nucleation and growth mechanisms of copper electrodeposition on bare and nitrogen-doped reduced graphene oxide modified SnO_2:F/glass substrates

G. Riveros[a,z], M. León[a,b], D. Ramírez[a], L. Hernández[a], F. Martín[c], R. Romero[d], E.A. Dalchiele[e].

[a]Instituto de Química y Bioquímica, Facultad de Ciencias, Universidad de Valparaíso, Avda. Gran Bretaña 1111, Playa Ancha, Valparaíso, Chile.

[b]Pontificia Universidad Católica de Valparaíso, Escuela de Ingeniería Química Av. Brasil, Nº 2180, Valparaíso, CL 2340000, Chile.

[c]Laboratorio de Materiales y Superficies (Unidad Asociada al CSIC). Departamentos de Física Aplicada & Ing. Química, Universidad de Málaga, E29071 Málaga, Spain.

[d]Nanotechnology Unit, Edificio de Bioinnovación, Universidad de Málaga, Málaga, Spain.

[e]Instituto de Física, Facultad de Ingeniería, Julio Herrera y Reissig 565, C.C. 30, 11000 Montevideo, Uruguay

[z]Corresponding Author

E-mail address: gonzalo.riveros@uv.cl

Phone: +56-32-2508175

Abstract

In this article, the influence of a nitrogen-doped electrochemically reduced graphene oxide layer on the nucleation and growth mechanisms of copper electrodeposition was studied. Thus, copper electrodeposition from an acidic solution was evaluated using two different substrates: fluorine-doped tin oxide (FTO), and fluorine-doped tin oxide covered with a nitrogen-doped reduced graphene oxide layer (FTO/N-ERGO). In both cases, chronoamperometric curves were obtained, which were analyzed and deconvoluted using pre-established models and equations, where the different contribution and nucleation parameters were determined. Field emission scanning electron microscopy (FESEM) images were acquired in order to observe the morphology and verify the nuclei density for each case considered in this study. In the case of copper electrodeposition onto FTO, an instantaneous three-dimensional nucleation was observed, together with a proton reduction reaction. When FTO/N-ERGO was used as a substrate, a new instantaneous two-dimensional nucleation process was observed in addition to the processes previously described. Furthermore, the increased density of active sites and the changes in copper morphology are directly related with the N-ERGO layer, which also increased the kinetic constant for the proton reduction reaction and the nucleation rate per active site during the copper electrodeposition process.

INTRODUCTION

Graphene, a two-dimensional allotrope of carbon, is an atomically flat monolayer of sp^2 hybridized carbon atoms arranged in a honeycomb lattice structure, with several interesting optoelectronic properties and a high surface area (2,630 m^2 g^{-1}).[1,2] To date, graphene and its derivatives (graphene oxide (GO), reduced graphene oxide (rGO)) are considered next-generation material for different optoelectronic devices.[1] In the last years, researchers have turned their attention to GO, which has the superb advantages of mass production and manageable solution processing capability.[3] GO can be viewed as graphene decorated with randomly distributed oxygen-containing functionalities on both sides of the basal plane and edges, i.e., epoxy and hydroxyl functional groups occupying the basal plane and carbonyl, carboxyl and lactol functionalities attached to the edges.[4–11] Through the removal of the attached oxygen functional groups from the planes and edges of GO via a reduction process, its electrical conductivity is restored to a certain degree.[3,12–14] In fact, the resulting rGO, which is formed after the thermal, chemical or electrochemical reduction of GO, possesses high charge carrier mobility, appreciable conductivity and has proven to be suitable as a two-dimensional semiconductor for functional electronic devices.[13] rGO has been considered a viable alternative candidate to that of ideal single-crystalline graphene because it can be produced on a large scale at a lower cost.[14]

Several reports have emerged that highlight the unique and sometimes unexpected optoelectronic properties of rGO-based thin films, providing prospects for their use in electronic devices such as integrated smart sensors, field emitters, solar cells, chem/bio-sensors, thin-film transistors, ultracapacitors and non-volatile

memory devices.[3,15–18] Recently, as an approach to obtain rGO, the electrochemical reduction of GO (to obtain electrochemically reduced graphene oxide (ERGO)) has emerged as a very beneficial approach, which has received more attention over other methods because it is simple, fast, low-cost, efficient, scalable and environmentally friendly.[11,13,19–22] Moreover, nitrogen-doping has been demonstrated to be an effective strategy for tailoring the unique electronic properties of graphene. GO can be easily doped with nitrogen atoms through the addition of melamine in an intermediate step during graphite oxidation based on the Hummers method.[23] Thus, nitrogen-doped graphene oxide (N-GO) is obtained, which can be reduced to nitrogen-doped reduced graphene oxide (N-rGO). This material has shown better electrical and catalytic properties than pristine graphene and has potential applications for sensors, electrocatalysts and electrochemical storage devices.[23–27]

Recently, many studies have been dedicated to the investigation of metals onto graphene surfaces, which aim to improve and manipulate graphene electronic and magnetic characteristics through metal atom adsorption or doping to satisfy the different demands of device applications.[28,29] The interest in growing metal nanostructures and thin films onto graphene is also supported by the fact that transition and noble metal nanostructures on graphene were shown to be efficient for supported catalysis.[28–35] There is also a technological interest in growing uniform magnetic metal films for spintronics or growing high density magnetic nanoparticles that are thermally stable for computer storage applications.[28,29] Furthermore, the study of metals onto graphene surfaces is essential in order to better understand the quality of metal contacts, a very critical issue for the performance of graphene-based

microelectronic and nanoelectronic devices.[28,29] In fact, the electronic properties of graphene are dramatically influenced by the interaction with metallic atoms.[28]

Thus, many efforts have been made to develop transition and noble metal thin films and nanostructures onto graphene substrates.[1,28,29] For instance, metal nanoparticles onto graphene surface heterostructures can be prepared using several methods such as chemical reduction, photochemical synthesis, microwave assisted synthesis, electroless metallization and physical vapor deposition processes.[28] In addition to these different preparation methods, electrochemical deposition is increasingly being used in the fabrication of complex metallic features with dimensions on deep-submicrometer levels.[36–40] Furthermore, due to its technological significance, the electrocrystallization of metal deposits on foreign substrates continues to command much interest in modern electrochemistry.[37] Thus, in order to achieve the precision required to produce nanometer-scale structures in a reliable and reproducible manner, this study will focus on the initial stages of the phase change which includes the formation and growth of the first nuclei of the new phase.[36–44]

A thorough review of the literature shows that among the narrow number of works dedicated to the electrodeposition of metals onto graphene surfaces, very few focus on nucleation and growth mechanisms, and these works are usually limited to the assessment of catalytic activity.[31–33] To the best of our knowledge, only three works can be found in the literature that study the nucleation and growth mechanisms of palladium,[34] lithium,[30] and copper[45] electrodeposition onto graphene or rGO. Furthermore, an exhaustive study of these mechanisms for copper does not

exist, which includes the effect of the graphene layer on the processes involved in the initial stages of metal electrodeposition.

This present study provides a fairly complete investigation of the nucleation and growth mechanisms of copper electrodeposition onto a nitrogen-doped electrochemically reduced graphene oxide (N-ERGO) surface. In this study, N-ERGO layers were obtained by the electrochemical reduction of N-GO onto an FTO electrode. The nucleation and growth mechanisms were deduced through analysis of chronoamperometric curves (j vs. t), and the results were compared with FESEM images of the electrodeposits obtained.

EXPERIMENTAL

All the chemicals reagents used in this study were of analytical grade and used without previous treatment. The solutions were prepared with deionized water (18.2 MΩ cm, Thermo Scientific, Branstead Easy Pure II). The electrochemical measurements were carried out in a conventional glass electrochemical cell with three electrodes: a working electrode (fluorine-doped tin oxide, FTO, in the absence and in the presence of a thin film of nitrogen-doped electrochemically reduced graphene oxide, N-ERGO); a counter electrode (platinum wire); and a reference electrode ($Ag/AgCl_{sat}$). All the potentials shown in this study are related to this reference electrode (0.199 V vs. SHE). Moreover, the electrochemical measurements were conducted in the absence of molecular oxygen for which the solutions were de-aerated with argon for 20 minutes. Afterwards, during the

electrochemical experiments, an argon stream was placed over the solution in order to prevent the presence of molecular oxygen. All the electrochemical measurements were carried out in an Autolab potentiostat-galvanostat (PGSTAT 302 N with a FRA32M module, controlled with NOVA software).

Nitrogen-doped graphene oxide (N-GO)

Nitrogen-doped graphene oxide (N-GO) was synthetized using the modified Hummers process, according to the previously reported in the literature.[23] Briefly, 1 g of graphite powder (mesh 350, Sigma-Aldrich) was mixed in an ice-water bath with 50 ml of concentrated sulfuric acid (Merck) and 0.5 g of $NaNO_3$ (Sigma-Aldrich). This mixture was stirred for 1 hour. After that, 3 g of $KMnO_4$ (Merck) were added to the mixture (several portions over a period of 4 hours). Next, 1 g of melamine (Sigma-Aldrich) was placed in the mixture and softly stirred over night at 30°C. Then, 50 ml of hot deionized water were added drop-to-drop, and the suspension was heated at 90°C for 1 hour. After that, 30 ml of 30% H_2O_2 (Merck) were added to the mixture and kept cool at room temperature. Then, the solid obtained was separated by decantation, and it was washed several times with deionized water. Finally, a concentrated suspension of N-GO (~ 12 g ml^{-1}, pH 3.00) was obtained.

Electrode cleaning and preparation

Before each measure, the electrode substrates were cleaned and adequately treated in order to obtain reproducible results. Thus, the FTO (TEC 15, XOP Glass, 12–14 Ω / sq) was cleaned successively with acetone (10 minutes) and ethanol (10

minutes) in an ultrasonic cleaner. For electrode surface modification, a thin film of N-ERGO was electrodeposited onto the FTO substrate forming a modified surface, FTO/N-ERGO. The electrodeposition process was carried out at constant potential (E = –0.85 V) for 5 minutes from a 1 mg ml^{-1} N-GO solution.[46] After that, the electrodes were washed with deionized water and used immediately as modified working electrodes when required.

Current transients (Chronoamperometric curves j vs. t) of copper electrodeposition onto FTO electrodes with and without N-ERGO film

Before carrying out the current transients, the corresponding voltammograms were obtained. These voltammograms, and the chronoamperometric curves, were obtained from a 0.01 M $CuSO_4$ solution, pH 1.00 (H_2SO_4). A potential interval, where the initial stages of copper electrodeposition are carried out, was defined according to the voltammetric responses. All the current transients were performed at constant potential for 60 s. The chronoamperometric curves were fitted through Microcal Origin software based on equations and models previously developed. Furthermore, the morphology of the samples obtained onto the FTO and FTO/N-ERGO electrodes was studied through FESEM images using a FEI Helios Nanolab 650 Dual Beam.

RESULTS AND DISCUSSION

Figure 1 shows the voltammetric response of a 0.01 M $CuSO_4$ acidic solution (pH 1.00) on both the FTO and modified FTO electrodes (FTO/N-ERGO; –0.85 V, 5 minutes, 1 mg lt^{-1} N-GO solution, pH 3.00).

In this Figure, a change in the cathodic scan response between the FTO and FTO/N-ERGO electrodes is observed. When an FTO/N-ERGO electrode is used, a displacement to more positive potentials for copper electrodeposition is obtained. The N-ERGO thin film deposited onto the FTO surface is responsible for this change. The film changes the electrode surface (insets in Figure 1), which affects the nucleation and growth mechanisms of copper onto these electrodes.[47] From the voltammetric responses, the potential intervals in which copper electrodeposition can be carried out, were determined for each electrode. Thus, in order to verify the effect of the N-ERGO thin film on the copper electrodeposition process onto FTO, current transients j vs. t onto both electrodes were obtained, as described in the experimental section. Figure 2 shows the current transients j vs. t for copper electrodeposition onto FTO and FTO/N-ERGO electrodes at different potentials.

As can be observed, the current density obtained on the FTO/N-ERGO electrodes are higher than those obtained on the same electrode without modification, which is independent of the applied potential. This can be a consequence of two factors: a superficial area increase, and a larger number of sites for copper nucleation from the solution. These factors are both effects of the FTO electrode superficial modification with the N-ERGO thin film. The first of these effects has already been studied, observing a current rise according to increases the superficial area of the electrode as a consequence of the formation of electrochemically reduced graphene layers.[48,49] The second effect is confirmed through a detailed analysis of the current transients j vs. t obtained onto both electrodes.

In order to establish a change in the nucleation mechanism onto the FTO and FTO/N-ERGO electrodes, dimensionless curves were drawn according to the equations developed by Scharifker and Hills.[50] In these cases, $(j / j_m)^2$ vs. (t / t_m) plots are obtained, where j_m and t_m are the current density and time maxima, respectively. These values are obtained directly from the current transients previously attained (Figure 2). The equation developed for an instantaneous three-dimensional nucleation with diffusional control (IN-3D nucleation) is:

$$\left(\frac{j}{j_m}\right)^2 = 1.9542\left(\frac{t_m}{t}\right)\left\{1-\exp\left[-1.2564\left(\frac{t}{t_m}\right)\right]\right\}^2 \quad (1)$$

Meanwhile, for a progressive three-dimensional nucleation with diffusional control (PG-3D nucleation) the equation is:

$$\left(\frac{j}{j_m}\right)^2 = 1.2254\left(\frac{t_m}{t}\right)\left\{1-\exp\left[-2.3367\left(\frac{t}{t_m}\right)^2\right]\right\}^2 \quad (2)$$

Figure 3 shows the results obtained from the dimensionless plots, $(j / j_m)^2$ vs. (t / t_m), for copper electrodeposition onto the FTO and FTO/N-ERGO electrodes from Figure 2. In this Figure, the theoretical curves for IN-3D and PG-3D nucleation with diffusional control are shown.

As can be observed, the dimensionless curves show that the copper electrodeposition onto an FTO electrode follows an IN-3D mechanism, like has been

previously reported.[51] However, in this study, a deviation from the theoretical IN-3D mechanism at time $t/t_m > 1$ is observed. This deviation is attributed to the proton reduction reaction as a consequence of the acidic medium and is catalyzed by copper clusters on the FTO surface. Thus, this reaction occurs once the first copper clusters are formed, and its contribution is appreciable at $t/t_m > 1$. However, when $t/t_m < 1$, the copper nucleation process prevails over the proton reduction reaction, because the formation of copper clusters is necessary before the proton reduction reaction occurs. This reaction has been reported previously for copper electrodeposition from an acidic solution onto different substrates,[52–55] as well as for the electrodeposition of other metals such as cobalt onto a glassy carbon electrode,[56] platinum onto FTO,[57] and palladium onto graphene.[34] At $t/t_m > 1$, this reaction provides a considerable contribution to the current during the copper electrodeposition process.[55] A similar behavior is observed for the current transients obtained onto the FTO/N-ERGO substrates (Figure 3 (b)). Although an IN-3D mechanism is observed for the FTO electrodes, a deviation from this mechanism at $t/t_m < 1$ can be appreciated for the FTO/N-ERGO electrode. Thus, while both electrodes demonstrate similar behavior, there is a variation in the nucleation mechanisms which is a consequence of the N-ERGO layer. This variation is discussed as a function of the different processes involved in copper nucleation (*vide infra*). In order to obtain a detailed effect of the changes produced by the N-ERGO layer in the nucleation mechanisms, the current transients were deconvoluted in the contributions considering copper electrodeposition and the proton reduction reaction. However, a cathodic current decay is observed once the potential pulse is applied, followed by the copper nucleation process. This process is evident at the

low electrodeposition overpotential and it turns negligible at high overpotentials (see Figure 2 (a) and (b)). The above is commonly observed in these kinds of studies and, in this case, is related to two consecutive monoelectronic steps:[58]

$$Cu^{2+}_{(aq)} + 1\bar{e} \rightarrow Cu^{+}_{(aq)} \quad (3)$$

$$Cu^{+}_{(aq)} + 1\bar{e} \rightarrow Cu_{(s)} \quad (4)$$

According to Milchev et al.[58], the cathodic current decay is attributed to the discharge of Cu^{2+} ions and the consequent Cu^{+} adsorption on the electrode (reaction (1)), which is kinetically slower than reaction (2). Thus, when the overpotential is low and there is a low current associated with the formation of copper nuclei, reaction (1) predominates over reaction (2), and an important contribution of the cathodic current decay is observed. On the other hand, when a high electrodeposition overpotential is applied, a high current associated with the formation of copper nuclei is observed, making the contribution of the current decay negligible. Thus, in order to carry out the deconvolution process, the cathodic current decay was subtracted from the global current in all of our measurements, using an exponential decay equation.[53] In the case of the FTO electrodes, the current transients are fitted considering the contribution of the instantaneous three-dimensional nucleation with diffusional control ($j_{(IN\text{-}3D)\text{-}diff}$) together with the proton reaction reduction (j_{PRR}). Although the copper electrodeposition process is a mechanism involving two consecutive monoelectronic steps,[58–60] for a nucleation and growth process under diffusional control, only the chemical specie under diffusional control (Cu^{2+} in

dissolution) and the formed solid phase (Cu^0 onto the FTO surface) are considered. Thus, the electrochemical process can be represented by the following reactions:

$$j_{(IN-3D)-diff}: \quad Cu^{2+}_{(aq)} + 2\bar{e} \rightarrow Cu_{(s)} \qquad (5)$$

$$j_{PRR}: \quad H^{+}_{(aq)} + 1\bar{e} \rightarrow H_{(ads)} \qquad (6)$$

For $j_{(IN\text{-}3D)\text{-}diff}$, the equation proposed by Scharifker and Mostany is used:[61]

$$j_{(IN-3D)-diff} = \frac{zFD^{1/2}C}{\pi^{1/2}t^{1/2}}\left[1-\exp(-N_0\pi kDt)\right], \qquad (7)$$

where $k = \left(\frac{8\pi MC}{\rho}\right)^{1/2}$

In this equation, z is the charge of the electrodeposited ion, F is the Faraday's constant, D is the diffusion coefficient of the electro-reduced ion ($cm^2\ s^{-1}$), C is the ion concentration (in mol cm^{-3}), N_0 is the number of active sites per unit area (cm^{-2}) and k is a dimensionless constant which depends on C, the density (ρ, g cm^{-3}) and the molecular weight (M, g mol^{-1}) of the material electrodeposited. Since the material electrodeposited is copper, D and C are referred to as the copper ion in dissolution

(Cu^{2+} ions, being $C = 1x10^{-5}$ mol cm^{-3}), while ρ and M are referred to as metallic copper (ρ = 8.96 g cm^{-3}, M = 63.546 g mol^{-1}), being z = 2.

On the other hand, for the current associated to the proton reduction reaction, the equation developed by Palomar-Pardavé et al. is used:[53,56]

$$j_{PRR} = z_{PRR} F k_{PRR} \left(\frac{2MC}{\pi\rho}\right)^{1/2} \left[1 - \exp\left\{-N_0 \pi k D \left(t - \frac{(1-\exp(-At))}{\Gamma}\right)\right\}\right] \quad (8)$$

In this equation, z_{PRR} is the proton ion charge, k_{PRR} is the kinetic constant for the proton reduction reaction (mol cm^{-2} s^{-1}), and A is the nucleation rate per active site (s^{-1}). The above equations can be represented in a simplified form by joining together terms, considering that the total current (j_{Total}) is the addition of $j_{(IN-3D)-diff}$ + j_{PRR}. Thus, the expression for the total current is as follows:

$$j_{Total} = \frac{P_1}{t^{1/2}}[1 - \exp(-P_2 t)] + P_3 \left[1 - \exp\left\{-P_2 \left(t - \frac{(1-\exp(-P_4 t))}{P_4}\right)\right\}\right], \quad (9)$$

where

$$P_1 = \frac{zFD^{1/2}C}{\pi^{1/2}}$$

$$P_2 = N_0 \pi k D$$

$$P_3 = z_{PRR} F k_{PRR} \left(\frac{2MC}{\pi\rho} \right)^{1/2}$$

$$P_4 = A$$

P_1 is a parameter independent of the potential and should be constant in all the measurements carried out. On the other hand, P_2, P_3 and P_4 are parameters dependent on the potential and should change according to the potential variation. Figure 4 shows the current transients, obtained at –40 mV and –100 mV (low and high electrodeposition overpotential, respectively), deconvoluted according to equation (9), and demonstrates a good correlation between the experimental data and the theoretical curves. Through deconvolution, the P_1, P_2, P_3 and P_4 parameters are obtained for each curve. Thus, the terms expressed in the previous equations can be calculated. This is summarized in Table 1.

As shown in Table 1, the diffusion coefficient D, obtained through parameter P_1, is essentially constant with an average value of 1.90×10^{-6} cm^2 s^{-1}, which is similar to the copper diffusion coefficient previously reported in the literature.[62] The differences found between these values can be attributed to a superficial inhomogeneity in the FTO substrate. Another way to determine D is through the Cottrell equation,[54,63] which can be rewritten as follows :[39,51]

$$D^{1/2} = \frac{\pi^{1/2}}{zFC} \left(\frac{\partial j}{\partial t^{-1/2}} \right) \qquad (10)$$

Thus, a plot j vs. $t^{-1/2}$ ($t >> t_m$, where a pure diffusion process is achieved) should present a line which passes from the origin and whose slope is used for the D determination. However, this equation cannot be used in this study because the proton reduction reaction is superimposed to copper electroreduction. Therefore, when the j vs. $t^{-1/2}$ curves were plotted, nonlinear curves were obtained, even at $t >> t_m$ (results not shown). Nevertheless, according to Scharifker and Hills,[50] for an instantaneous three-dimensional nucleation, the diffusion coefficient can also be determined by:

$$D = \frac{j_m^2 t_m}{0.163(zFC)^2} \tag{11}$$

According to this equation, the product $j_m^2 t_m$ should be constant for and independent of the electrodeposition overpotential. Table 2 shows the values of j_m, t_m, and $j_m^2 t_m$ obtained from the chronoamperometric curves of copper electrodeposition onto FTO at different potentials (Figure 2 (a)), and the diffusion coefficient obtained through these values using equation (11).

As can be observed, the product $j_m^2 t_m$ is not constant in the potential interval studied and provides different D values, although, in the same order as those obtained through the chronoamperometric curve deconvolution. The differences between the $j_m^2 t_m$ values are associated with the proton reduction reaction, which is present even in the initial stages of the copper electrodeposition process. The aforementioned is confirmed in Figure 4, which shows that the proton reduction

reaction occurs together with the copper electrodeposition process during the whole-time interval, affecting the j_m and t_m values of the experimental chronoamperometric curves. Thus, equations (10) and (11) can only be used when the electrodeposition process occurs in the absence of any other additional electrochemical process. In conclusion, the D values shown in Table 1 are considered appropriate for this study, using the average value (1.90×10^{-6} cm^2 s^{-1}) for the determination of N_0 from the P_2 parameter. On the other hand, the parameters P_2, P_3 and P_4 are electrodeposition potential dependent. Thus, N_0, k_{PRR} and the nucleation rate per active site A (associated with the P_2, P_3 and P_4 parameters, respectively) rise with the electrodeposition overpotential (to more negative potentials).

As in the case of the diffusion coefficient, N_0 can also be determined through the model developed by Scharifker and Hills.[50] Thus, the following equation is used for an instantaneous three-dimensional nucleation:[51,54,55,63]

$$N_0 = 0.065\left(\frac{\rho}{8\pi CM}\right)\left(\frac{zFC}{j_m t_m}\right)^2 \qquad (12)$$

As opposed to the diffusion coefficient determination, the product $j_m t_m$ is not constant and is potential dependent. However, as previously discussed, the j_m and t_m values obtained from the experimental chronoamperometric curves, including the contribution of the proton reduction reaction, affect the use of these parameters for the determination of the number of active sites. Thus, the N_0 values from Table 1 are considered adequate for this study, which coincide with those previously determined from copper electrodeposition onto FTO.[51] Using these values, it is possible to obtain

the dependence of N_0 on the potential, which is shown in Figure 5. As can be observed, there is a linear dependence between the logarithm of N_0 and the potential, which is consistent with the classical electrochemical nucleation model, where $N_0 \alpha \exp(-e\Delta U/kT)$.[39,51,55]

In order to observe the number and morphology of formed copper nuclei, FESEM images of the FTO surfaces were obtained before and after electrodeposition at different potentials (Figure 6). As can be observed, the copper nuclei number is practically constant at different electrodeposition potentials (see Figure 6 (b)–(f)). This can be a consequence of the same copper nuclei acting as new nucleation centers, which is known as the renucleation process. This process has been previously observed for copper electrodeposition from an acidic solution onto both tantalum[64] and ruthenium oxide in the presence of additives.[38] In both cases, the irregular shapes of the copper clusters are related to this phenomenon, which is consistent with the shape of the copper crystals observed in Figure 6. Thus, no new nuclei could be observed on the FTO surface, even at high electrodeposition overpotentials. A nuclei growth is only observed as more negative electrodeposition potential is applied (compare Figure 6 (b) with Figure 6 (f)). Furthermore, the copper cluster density was obtained for each potential studied by employing low magnification FESEM images (not shown) and, in all cases, shows a good correlation between these values and the N_0 values obtained from the deconvolution of the current transients.

The dependence of k_{PRR} and A on the electrodeposition potential is shown in Figure 7. In the case of k_{PRR}, which is associated with the proton reduction reaction

(see equation (8)), a linear dependency is obtained. Thus, a Butler-Vomer relationship can be assumed through the following equation:

$$k_{PRR} = k_{PRR}^{0} \exp\left(\frac{-\alpha_{PRR} z_{PRR} FE}{RT}\right) \tag{13}$$

where k_{HRR}^{0} is the standard heterogeneous kinetic constant for the proton reduction reaction, α_{PRR} is the transfer coefficient for this reaction, R is the gas constant (in J mol^{-1} K^{-1}) and E is the applied potential.

Using the equation above, and the appropriate values for each term, a value of 0.28 is obtained for α_{PRR}. This value is higher than those determined for the proton reduction reaction (α_{PRR} = 0.14) during palladium electrodeposition onto graphene,[34] but slightly smaller than the value determined by Palomar-Pardavé et al.[56] for cobalt electrodeposition (α_{PRR} = 0.32). On the other hand, considering the atomistic theory of electrochemical nucleation,[65–67] A is related to the potential through the following equation:

$$A = k' \exp\left(-\frac{W_k}{kT}\right) \exp\left(\frac{\alpha z e_0 \eta}{kT}\right) \tag{14}$$

where k' is the pre-exponential factor, W_k is the reversible work for the critical nucleus formation (which is associated to n_k, the number of atoms forming this nucleus), α is

the cathodic transfer coefficient, η is the overpotential imposed, e_0 is the elementary electric charge, k is the Boltzmann's constant, and T is the absolute temperature.

Considering the above-mentioned, a linear relationship between lnA and the potential is expected, as shown in Figure 7 (b).

In order to compare the N-ERGO layer effect on copper electrodeposition, curves from Figure 2 (b) (copper electrodeposition onto the FTO/N-ERGO electrodes) were deconvoluted. In Figure 3, where similar dimensionless curves are obtained for copper electrodeposition onto both FTO electrodes in the presence and in the absence of the N-ERGO layer, equation (9) was used in order to deconvolute the chronoamperometric curves obtained in Figure 2 (b) (FTO/N-ERGO electrode). However, this was not possible due to the presence of another nucleation process in the initial stages of the copper electrodeposition process. In this way, an adequate fitting was reached considering a new process besides that described in equation (9). This process was an instantaneous two-dimensional nucleation (IN-2D nucleation) and, according to the Bewick-Fleischmann-Thirsk (BFT) model, is described by the following equation:[68]

$$j_{(IN-2D)} = \frac{2z\pi FMhN_{0-2D}k_{2D}^{2}t}{\rho}\left[\exp\left(-\frac{\pi N_{0-2D}M^{2}k_{2D}^{2}t^{2}}{\rho^{2}}\right)\right] \quad (15)$$

Here, the new parameters are the two-dimensional nuclei height h (cm), the density of active sites for IN-2D nucleation per unit area $N_{0\text{-}2D}$ (cm^{-2}) and the rate constant for the two-dimensional nuclei growth k_{2D} ($mol\ cm^{-2}\ s^{-1}$). Thus, adding

equation (15) to equation (9), equation (16) is obtained, which is used to deconvolute the current transients of copper electrodeposition onto the FTO/N-ERGO electrodes:

$$j_{Total} = \frac{P_1}{t^{1/2}}\left[1-\exp(-P_2 t)\right] + P_3\left[1-\exp\left\{-P_2\left(t-\frac{(1-\exp(-P_4 t))}{P_4}\right)\right\}\right] + P_5\, t\left[\exp(-P_6 t^2)\right]$$

(16)

where

$$P_5 = \frac{2z\pi FMhN_{0-2D}k_{2D}^2}{\rho}$$

$$P_6 = \frac{\pi N_{0-2D}M^2k_{2D}^2}{\rho^2}$$

Figure 8 shows the deconvolution of the current transients obtained for copper electrodeposition onto the FTO/N-ERGO electrodes at low and high electrodeposition overpotentials, –20 mV and –80 mV, respectively. As can be observed in both cases, there is a good correlation between the theorical curves described by equation (16) and the experimental results. The deconvolution results of the current transients for copper electrodeposition onto the FTO/N-ERGO electrodes are summarized in Table 3 (*vide infra)*.

As can be deduced, the instantaneous two-dimensional nucleation process is a consequence of the N-ERGO layer formed onto the FTO surface. In this case, the N-ERGO layers cover the FTO surface forming both a flat-smooth surface and the

N-ERGO layer folds, which can act as new centers for copper nucleation (*vide infra,* Figure 11 (a)). Thus, the flat-smooth surfaces act as centers for IN-2D copper nucleation, whereas the folds will act as new centers for IN-3D copper nucleation. The presence of a 2D nucleation together with a 3D nucleation has been previously observed during copper electrodeposition from an acidic solution in the presence of chloride ions onto both platinum and poly-3-methylthiophene modified platinum electrodes.[69] As in this study, the IN-2D nucleation can be associated to the reduction of Cu^{2+} ions adsorbed onto the N-ERGO surface. The adsorption process of Cu^{2+} and other ions onto the ERGO and GO surfaces has been widely studied in order to use these materials as active material for the removal and recovery of metal ions.[70,71] The adsorption capability of ERGO (and similar materials such as GO) is dependent on many factors: pH, temperature, the ERGO reduction degree, among others. Thus, the physical contact between N-ERGO and the electrolyte can easily form adsorbed Cu^{2+} ions onto the surface of this material through the interaction between Cu^{2+} and the oxygenated functional groups (especially carboxyl groups) present on the N-ERGO surface.[70] These adsorbed ions are reduced independent of the copper from the dissolution, through a two-dimensional process. If the above is true, a constant reduction electric charge (Q) should be obtained independent of the potential reduction. Using the deconvolution results, the electric charges of the IN-2D processes at different electrodeposition potentials are obtained, which are shown in Figure 9 (a). As can be observed, electric charges for the IN-2D process between –0.803 and –0.854 mC cm^{-2} are obtained. These values can be considered as constant, assuming that the FTO/N-ERGO surface is not totally reproducible between each measurement, and little changes between a surface and another can

be expected. However, the electric charges shown in Figure 9 (a) are bigger than those expected for a copper monolayer (–0.420 mC cm^{-2}).[72] Effectively, this value is expected for a full copper monolayer onto a flat and smooth surface. But, in our case, FTO and FTO/N-ERGO are not flat and smooth surfaces (*vide infra*, Figures 11 (a)–(f)), and electric charges bigger than –0.420 mC cm^{-2} can be obtained. On the other hand, the N-ERGO deposited onto the FTO surface is not a monolayer, it is an ensemble of piled N-ERGO layers. In this way, Cu^{2+} ions are adsorbed onto different N-ERGO layers, and not only on the exposed face of the N-ERGO. Thus, when copper electroreduction takes place, all the Cu^{2+} ions adsorbed on the different N-ERGO layers are reduced, obtaining electric charges bigger than those required for a monolayer formation on a smooth surface.

According to the BFT model, the dependence of j_m and t_m for an IN-2D process on the potential must obey the following equation:[73]

$$\frac{\partial\left[\ln\left(-j_m\right)\right]}{\partial E} = -\frac{\partial\left[\ln\left(t_m\right)\right]}{\partial E} \qquad (17)$$

In Figure 9 (b) the relationship between $\ln(-j_m)$ and $\ln(t_m)$ on the potential is shown in a semilogarithmic scale. As can be observed, in both cases a linear correlation is obtained. Besides, the slope values in each case are -19.49 ± 2.70 for $\ln(-j_m)$ vs. E and 18.66 ± 2.54 for $\ln(t_m)$ vs. E, which confirms the validity of equation (17), and justifies the presence of the IN-2D nucleation during copper electrodeposition onto the FTO/N-ERGO electrodes. In this way, the presence of the IN-2D process in the initial stages of the copper electrodeposition process ($t < t_m$) is

responsible for the deviation found in the plot of dimensionless curves for copper electrodeposition onto the FTO/N-ERGO surface (Figure 2 (b)), where higher than expected currents in the theoretical curves were obtained.

According to the values obtained through the deconvolution shown in Table 3, parameters P_5 and P_6 are obtained. Both parameters are dependent on $N_{0\text{-}2D}$ and k_{2D}, which are in turn potential dependent, as shown in Table 3. Besides, from parameters P_5 and P_6, the height of two-dimensional nuclei, h, can be determined. In our case, h was practically constant, varying from 2.95 Å at –20 mV to 3.10 Å at –100 mV, confirming the validity of the deconvolution processes carried out. Similar results have been reported for copper under potential deposition onto Au nanoparticles supported onto an ITO electrode.[74] However, these values are higher than a copper monolayer (2.56 Å), as expected and previously discussed.

The parameter P_1 values obtained in Table 3 are slightly higher than those obtained in Table 1, although all the terms in P_1 are independent of the FTO modification. This is attributed to an increase in the superficial area of the FTO electrode as a consequence of the N-ERGO layer. In order to explain this difference, it is necessary to consider that the current density was determined using the electrode geometrical area (A_G) and that the superficial area is equal to the geometrical area multiplied by factor F_{SA} (where $F_{SA} > 1$). Thus, P_1 can be rewritten in function of the superficial area as:

$$P_1 = \frac{zFD^{1/2}CA_GF_{SA}}{\pi^{1/2}} \qquad (18)$$

Thus, according to our results

$$P_{1-FTO/NERGO} > P_{1-FTO} \qquad (19)$$

$$\frac{zFD^{1/2}CA_{G-FTO/NERGO}F_{SA-FTO/NERGO}}{\pi^{1/2}} > \frac{zFD^{1/2}CA_{G-FTO}F_{SA-FTO}}{\pi^{1/2}} \qquad (20)$$

Considering two electrodes (an FTO electrode and an FTO electrode covered with a N-ERGO layer) with the same geometrical area ($A_{G-FTO/NERGO} = A_{G-FTO}$), all the terms of the above equation will be the same, except F_{SA}. Thus:

$$F_{SA-FTO/NERGO} > F_{SA-FTO} \qquad (21)$$

In this way, for two electrodes with the same geometrical area but with a different superficial area, different P_1 values will be expected, as in our case.

On the other hand, the P_1 values obtained in Table 3 remain essentially constant in the potential interval studied, where the slight differences found are attributed to the N-ERGO layer inhomogeneity between each measurement. This tendency is reflected in the diffusion coefficient obtained. However, since the difference of the copper diffusion coefficient values obtained between the FTO and FTO/N-ERGO electrodes is related to an area difference, the value of copper electrodeposition onto FTO is considered appropriate for this study. As in the previous case, the diffusion coefficient cannot be determined through equations (10)

and (11) because of the presence of both the IN-2D nucleation process and the hydrogen reduction reaction during the initial stages of copper electrodeposition.

On the other hand, parameters P_2 and N_0 increase with the electrodeposition overpotential, as expected. When comparing these values with those obtained from copper electrodeposition onto FTO (P_2 and N_0 in Table 1), the parameter values onto the FTO/N-ERGO electrodes are one magnitude order higher than those obtained onto the FTO electrodes. This is related to both the higher density of active centers for copper nucleation as a consequence of the N-ERGO folds, and the presence of two-dimensional nuclei, as previously mentioned. Furthermore, these centers are activated with the electrodeposition overpotential which is consistent with the suggested models.[68] Figure 10 shows the dependence of N_0 on the potential obtained through the values acquired from Table 3.

As in the case of copper electrodeposition onto the FTO electrodes, the dependence of N_0 on the electrodeposition potential is related to the classical electrochemical nucleation model.[39,51,55]

On the other hand, FESEM images of the copper deposits (Figure 11 (b)–(f)) demonstrate that copper nuclei density increases with the electrodeposition overpotential. However, considering that the height of a two-dimensional nucleus is the same height as a copper atom, it not possible to observe the presence of two-dimensional nuclei in the FESEM images because the resolution of this technique does not reach atomic levels. Thus, only three-dimensional nuclei are observed. In these images, it is also possible to observe that the nuclei morphology changes (insets in Figure 11 (b)–(f)) obtaining crystalline deposits with sharp edges at low electrodeposition overpotentials (–20 mV and –40 mV) and globular particles at high

electrodeposition overpotentials (–60 mV and –80 mV), similar to the findings obtained by Wu et al.[45] The latter form small crystals, which are evident in the insets of Figures 11 (e) and 10 (f). As in the case of the FTO substrates, good correlations between the copper cluster densities, obtained from low magnification FESEM images and the N_0 values obtained from the deconvolution of the current transients, were obtained. This shows that the nucleation model proposed in each case is consistent with the results obtained.

Parameter P_3, which is related to the proton reduction reaction kinetic, also increases with the electrodeposition overpotential, as expected (see Figure 12 (a)). Compared with the same parameter obtained for the FTO electrodes (P_3 in Table 1), this value is larger, which is attributed to a change in copper morphology. In this case, the copper deposit is formed by small crystals which are different from those formed in the absence of the N-ERGO layer (compare insets in Figure 11 with Figure 6). These small crystals are responsible for the high proton reduction kinetic observed in comparison to the smooth copper surfaces obtained when it is formed onto the FTO electrodes.

Finally, parameter P_4, which corresponds to the nucleation rate per active site A, also increases with the electrodeposition overpotential (Figure 12 (b)), and it is higher than the same parameter obtained for an FTO electrode (P_4 in Table 1), as discussed above.

1. CONCLUSIONS

This study shows the changes that produce the electro-formation of a N-ERGO layer onto an FTO surface in the nucleation and growth mechanisms of copper electrodeposition from an acidic solution. Thus, when an FTO electrode in the absence of a N-ERGO layer was used as a substrate, when analyzing the chronoamperometric curves (j vs. t) of copper electrodeposition, an instantaneous three-dimensional nucleation together with a proton reduction reaction was observed. However, when an FTO surface modified with an FTO/N-ERGO layer was used as a substrate, a new instantaneous two-dimensional nucleation process was observed in addition to the processes previously named. This two-dimensional process is attributed to the reduction of Cu^{2+} ions adsorbed onto the different N-ERGO layers formed onto the FTO surface, which are formed through contact between the FTO/N-ERGO substrate with the electrolytic dissolution. The electric charge of reduction associated with this two-dimensional nucleation is practically constant between each measurement, which varies between –0.803 and –0.854 mC cm^{-2}. Besides, the relationship between $-j_m$ and t_m of this two-dimensional process with the electrodeposition potential obeys the BFT model, which validates our results. On the other hand, the N-ERGO layer forms folds onto the FTO surface, which, together with the two-dimensional nuclei previously formed, act like new active sites for copper nucleation. Thus, an increase of N_0 with respect to the FTO substrate is observed. Through FESEM images, a change in copper morphology was also evidenced. Thus, smooth surface copper nuclei were obtained when copper was electrodeposited onto FTO surfaces in the absence of a N-ERGO layer, and globular particles forming small crystals were observed, when copper was electrodeposited onto an FTO electrode in the presence of a N-ERGO layer. These

small crystals are responsible for increasing the kinetics of the proton reduction reaction observed during copper electrodeposition onto the FTO/N-ERGO electrodes.

Acknowledgements

This work was funded by FONDECYT (Chile), project number 1160952. E.A.D would like to acknowledge PEDECIBA-Física (Montevideo, Uruguay) for their support. F.M. would also like to acknowledge the Ministry of Economy and Competitiveness of Spain (TEC2014-53906) for their support.

REFERENCES

1. M. Batzill, *Surf. Sci. Rep.*, **67**, 83 (2012).

2. W. Gao, *Graphene oxide: Reduction recipes, spectroscopy, and applications* W. Gao, Editor, p. 1–147, Springer International Publishing, Cham, (2015).

3. A. G. Marrani, A. Motta, R. Schrebler, R. Zanoni, and E. A. Dalchiele, *Electrochim. Acta*, **304**, 231 (2019).

4. W. Gao, L. B. Alemany, L. Ci, and P. M. Ajayan, *Nat. Chem.*, **1**, 403 (2009).

5. S. C. Ray, in *Applications of Graphene and Graphene-Oxide Based Nanomaterials*,, p. 39–55, William Andrew Publishing (2015).

6. G. Eda, C. Mattevi, H. Yamaguchi, H. Kim, and M. Chhowalla, *J. Phys. Chem. C*, **113**, 15768 (2009).

7. B. Li, G. Pan, N. D. Avent, R. B. Lowry, T. E. Madgett, and P. L. Waines, *Biosens.*

Bioelectron., **72**, 313 (2015).

8. C. Gómez-Navarro, J. C. Meyer, R. S. Sundaram, A. Chuvilin, S. Kurasch, M. Burghard, K. Kern, and U. Kaiser, *Nano Lett.*, **10**, 1144 (2010).

9. A. Mathkar, D. Tozier, P. Cox, P. Ong, C. Galande, K. Balakrishnan, A. Leela Mohana Reddy, and P. M. Ajayan, *J. Phys. Chem. Lett.*, **3**, 986 (2012).

10. T. Kuila, S. Bose, A. K. Mishra, P. Khanra, N. H. Kim, and J. H. Lee, *Prog. Mater. Sci.*, **57**, 1061 (2012).

11. C. N. Hernández, M. B. G. García, D. H. Santos, M. A. Heras, A. Colina, and P. Fanjul-Bolado, *Electrochem. Commun.*, **64**, 65 (2016).

12. A. G. Marrani, A. C. Coico, D. Giacco, R. Zanoni, F. A. Scaramuzzo, R. Schrebler, D. Dini, M. Bonomo, and E. A. Dalchiele, *Appl. Surf. Sci.*, **445**, 404 (2018).

13. A. G. Marrani, R. Zanoni, R. Schrebler, and E. A. Dalchiele, *J. Phys. Chem. C*, **121**, 5675 (2017).

14. M. F. Abdullah, S. F. Abd Rahman, and A. M. Hashim, *Phys. Status Solidi A*, **216**, 1900064 (2019).

15. G. C. Xie, K. Zhang, B. D. Guo, Q. Liu, L. Fang, and J. R. Gong, *Adv. Mater.*, **25**, 3820 (2013).

16. G. Eda, and M. Chhowalla, *Adv. Mater.*, **22**, 2392 (2010).

17. G. Li, L. Liu, G. Wu, W. Chen, S. Qin, Y. Wang, and T. Zhang, *Small*, **12**, 5019 (2016).

18. M. Belekoukia, M. S. Ramasamy, S. Yang, X. Feng, G. Paterakis, V. Dracopoulos, C. Galiotis, and P. Lianos, *Electrochim. Acta*, **194**, 110 (2016).

19. S. Y. Toh, K. S. Loh, S. K. Kamarudin, and W. R. W. Daud, *Chem. Eng. J.*, **251**, 422 (2014).

20. Y. Joo, M. S. Ahmed, H. S. Han, and S. Jeon, *Int. J. Hydrog. Energy*, **42**, 21751 (2017).

21. A. Viinikanoja, J. Kauppila, P. Damlin, M. Suominen, and C. Kvarnström, *Phys. Chem. Chem. Phys.*, **17**, 12115 (2015).

22. D. P. Rocha, R. M. Dornellas, R. M. Cardoso, L. C. D. Narciso, M. N. T. Silva, E. Nossol, E. M. Richter, and R. A. A. Munoz, *Sens. Actuators B Chem.*, **254**, 701 (2018).

23. M. Du, J. Sun, J. Chang, F. Yang, L. J. Shi, and L. Gao, *RSC Adv.*, **4**, 42412 (2014).

24. G. Li, Z. Li, X. Xiao, Y. An, W. Wang, and Z. Hu, *J. Mater. Chem. A*, **7**, 11077 (2019).

25. Z. Y. Lin, G. H. Waller, Y. Liu, M. L. Liu, and C. P. Wong, *Carbon*, **53**, 130 (2013).

26. Z. L. Ma, X. B. Huang, S. Dou, J. H. Wu, and S. Y. Wang, *J. Phys. Chem. C*, **118**, 17231 (2014).

27. P. H. Zhao, W. L. Li, G. Wang, B. Z. Yu, X. J. Li, J. T. Bai, and Z. Y. Ren, *J. Alloys Compd.*, **604**, 87 (2014).

28. F. Ruffino, and F. Giannazzo, *Crystals*, **7**, 219 (2017).

29. X. Liu, C. Z. Wang, M. Hupalo, W. C. Lu, M. C. Tringides, Y. X. Yao, and K. M. Ho, *Phys. Chem. Chem. Phys.*, **14**, 9157 (2012).

30. Q. Meng, B. Deng, H. Zhang, B. Wang, W. Zhang, Y. Wen, H. Ming, X. Zhu, Y. Guan, Y. Xiang, M. Li, G. Cao, Y. Yang, H. Peng, H. Zhang, and Y. Huang, *Energy Stor. Mater.*, **16**, 419 (2019).

31. C. Te Hsieh, J. M. Wei, H. T. Hsiao, and W. Y. Chen, *Electrochim. Acta*, **64**, 177 (2012).

32. C. Te Hsieh, J. M. Wei, J. S. Lin, and W. Y. Chen, *Catal. Commun.*, **16**, 220 (2011).

33. C. Te Hsieh, Y. Y. Liu, and A. K. Roy, *Electrochim. Acta*, **64**, 205 (2012).

34. M. Rezaei, S. H. Tabaian, and D. F. Haghshenas, *Electrochim. Acta*, **87**, 381 (2013).

35. Y. Ioni, E. Buslaeva, and S. Gubin, *Mater. Today Proc.*, **3**, S209 (2016).

36. A. Milchev, *Contemp. Phys.*, **32**, 321 (1991).

37. M. Palomar-Pardavé, M. Miranda-Hernández, I. González, and N. Batina, *Surf. Sci.*, **399**, 80 (1998).

38. L. Guo, A. Radisic, and P. C. Searson, *J. Electrochem. Soc.*, **153**, C840 (2006).

39. W. Shao, G. Pattanaik, and G. Zangari, *J. Electrochem. Soc.*, **154**, D339 (2007).

40. L. Santinacci, T. Djenizian, P. Schwaller, T. Suter, A. Etcheberry, and P. Schmuki, *J. Phys. D*, **41**, 9 (2008).

41. H. Gómez, R. Henríquez, R. Schrebler, R. Córdova, D. Ramírez, G. Riveros, and E. A. Dalchiele, *Electrochim. Acta*, **50**, 1299 (2005).

42. G. Riveros, D. Ramirez, A. Tello, R. Schrebler, R. Henriquez, and H. Gomez, *J. Braz. Chem. Soc.*, **23**, 505 (2012).

43. E. C. Muñoz, R. S. Schrebler, R. A. Córdova, R. E. Marotti, and E. A. Dalchiele, *J. Phys. Chem. C*, **111**, 16506 (2007).

44. S. Bijani, R. Schrebler, E. A. Dalchiele, M. Gabás, L. Martínez, and J. R. Ramos-Barrado, *J. Phys. Chem. C*, **115**, 21373 (2011).

45. S. Wu, Z. Yin, Q. He, G. Lu, Q. Yan, and H. Zhang, *J. Phys. Chem. C*, **115**, 15973 (2011).

46. R. Carrizo, D. Ramírez, L. Hernández, G. Lobos, P. Häberle, E. A. Dalchiele,

and G. Riveros, *ChemElectroChem*, **6**, 1047 (2019).

47. T. Rapecki, M. Donten, A. M. Nowicka, and Z. Stojek, *J. Electroanal. Chem.*, **677–680**, 83 (2012).

48. Y. Y. Jiang, Y. Z. Lu, F. H. Li, T. S. Wu, L. Niu, and W. Chen, *Electrochem. Commun.*, **19**, 21 (2012).

49. C. Liu, K. Wang, S. Luo, Y. Tang, and L. Chen, *Small*, **7**, 1203 (2011).

50. B. Scharifker, and G. Hills, *Electrochim. Acta*, **28**, 879 (1983).

51. M. R. Khelladi, L. Mentar, A. Azizi, A. Sahari, and A. Kahoul, *Mater. Chem. Phys.*, **115**, 385 (2009).

52. D. Arrington, M. Curry, S. Street, G. Pattanaik, and G. Zangari, *Electrochim. Acta*, **53**, 2644 (2008).

53. E. Garfias-García, M. Romero-Romo, M. T. Ramírez-Silva, and M. Palomar-Pardavé, *Int. J. Electrochem. Sci.*, **7**, 3102 (2012).

54. D. Grujicic, and B. Pesic, *Electrochim. Acta*, **47**, 2901 (2002).

55. A. Radisic, J. G. Long, P. M. Hoffmann, and P. C. Searson, *J. Electrochem. Soc.*, **148**, C41 (2002).

56. M. Palomar-Pardavé, B. R. Scharifker, E. M. Arce, and M. Romero-Romo, *Electrochim. Acta*, **50**, 4736 (2005).

57. Y. S. Ko, and Y. U. Kwon, *Electrochim. Acta*, **55**, 7276 (2010).

58. A. Milchev, and T. Zapryanova, *Electrochim. Acta*, **51**, 2926 (2006).

59. W. Shao, G. Pattanaik, and G. Zangari, *J. Electrochem. Soc.*, **154**, D201 (2007).

60. M. A. Pasquale, L. M. Gassa, and A. J. Arvia, *Electrochim. Acta*, **53**, 5891 (2008).

61. B. R. Scharifker, and J. Mostany, *J. Electroanal. Chem.*, **177**, 13 (1984).

62. L. O. S. Bulhões, and L. H. Mascaro, *J. Solid State Electrochem.*, **8**, 238 (2004).

63. D. Grujicic, and B. Pesic, *Electrochim. Acta*, **50**, 4426 (2005).

64. A. Radisic, G. Oskam, and P. C. Searson, *J. Electrochem. Soc.*, **151**, C369 (2004).

65. H. Cesiulis, and M. Ziomek-Moroz, *J. Appl. Electrochem.*, **30**, 1261 (2000).

66. A. Milchev, *Contemp. Phys.*, **32**, 321 (1991).

67. M. Palomar-Pardavé, M. T. Ramírez, I. González, A. Serruya, and B. R. Scharifker, *J. Electrochem. Soc.*, **143**, 1551 (1996).

68. D. Pletcher, R. Greff, R. Peat, L. M. Peter, and J. Robinson, in *Instrumental Methods in Electrochemistry*, D. Pletcher, R. Greff, R. Peat, L. M. Peter, and J. B. T. Robinson, Editors, p. 283–316, Woodhead Publishing, Cambridge (2001).

69. M. R. Guascito, C. Malitesta, and L. Sabbatini, *Mater. Chem. Phys.*, **131**, 719 (2012).

70. B. Wang, F. Zhang, S. He, F. Huang, and Z. Peng, *Asian J. Chem.*, **26**, 4901 (2014).

71. S. Yang, L. Li, Z. Pei, C. Li, X. Q. Shan, B. Wen, S. Zhang, L. Zheng, J. Zhang, Y. Xie, and R. Huang, *Carbon*, **75**, 227 (2014).

72. A. I. Danilov, J. E. T. Andersen, E. B. Molodkina, Y. M. Polukarov, P. Møller, and J. Ulstrup, *Electrochim. Acta*, **43**, 733 (1997).

73. M. H. Hölzle, U. Retter, and D. M. Kolb, *J. Electroanal. Chem.*, **371**, 101 (1994).

74. J. Aldana-González, J. Olvera-García, M. G. Montes De Oca, M. Romero-Romo, M. T. Ramírez-Silva, and M. Palomar-Pardavé, *Electrochem. Commun.*, **56**, 70 (2015).

TABLE 1

Table 1: The P_1, P_2, P_3 and P_4 parameters expressed in equation (9), and the values of A, D, N_0 and k_{PRR} obtained through the deconvolutions of the current transients of copper electrodeposition onto FTO electrodes at different potentials (Figure 2 (a)).

E / mV	**P_1 / $mA\ cm^{-2}\ s^{1/2}$**	**P_2 / s^{-1}**	**P_3 / $mA\ cm^{-2}$**	**P_4 (A) / s^{-1}**	**D x10^6 / $cm^2\ s^{-1}$**	**N_0 x 10^{-5} / cm^{-2}**	**k_{PRR} x10^7 / $mol\ cm^{-2}\ s^{-1}$**
–40	1.46	0.122	0.0901	0.0160	1.80	4.83	1.39
–60	1.46	0.189	0.1100	0.0397	1.80	7.50	1.70
–80	1.46	0.350	0.1455	0.105	1.80	13.9	2.25
–100	1.60	0.481	0.1686	0.235	2.16	19.1	2.61

TABLE 2

Table 2: The j_m, t_m values and the product $j_m^2 t_m$ obtained from the chronoamperometric curves of copper electrodeposition onto FTO electrodes at different potentials. Using the appropriate values of z, F and C in equation (11), the diffusion coefficient D is calculated.

E / mV	**j_m / mA cm^{-2}**	**t_m / s**	**$j_m^2 t_m$ / (mA cm^{-2})^2 s**	**D x10^6 / cm^2 s^{-1}**
–40	0.338	12.1	1.38	2.28
–60	0.425	9.20	1.66	2.74
–80	0.585	4.95	1.69	2.79
–100	0.769	2.89	1.71	2.82

TABLE 3

Table 3: The P_1, P_2, P_3, P_4, P_5 and P_6 parameters expressed in equation (16), and the values of A, D, N_0 and k_{PRR} obtained through the deconvolutions of the current transients of copper electrodeposition onto the FTO/N-ERGO electrodes at different potentials (Figure 2 (b)).

E / mV	**P_1 / mA cm^{-2} s$^{1/2}$**	**P_2 / s^{-1}**	**P_3 / mA cm^{-2}**	**P_4 (A) / s^{-1}**	**P_5 / mA cm^{-2} s^{-1}**	**P_6 / s^{-2}**	**D x10^6 / cm^2 s^{-1}**	**N_0 x10^{-5} / cm^{-2}**	**k_{PRR} x10^7 / mol cm^{-2} s^{-1}**
–20	1.75	0.18	0.207	0.0153	0.00450	0.0028	2.58	7.19	3.19
–40	1.83	0.372	0.235	0.0342	0.0138	0.0082	2.82	14.8	3.62
–60	1.72	1.09	0.252	0.224	0.0186	0.0109	2.50	43.1	3.89
–80	1.62	2.25	0.285	0.524	0.0510	0.0302	2.21	89.3	4.39

FIGURE 1

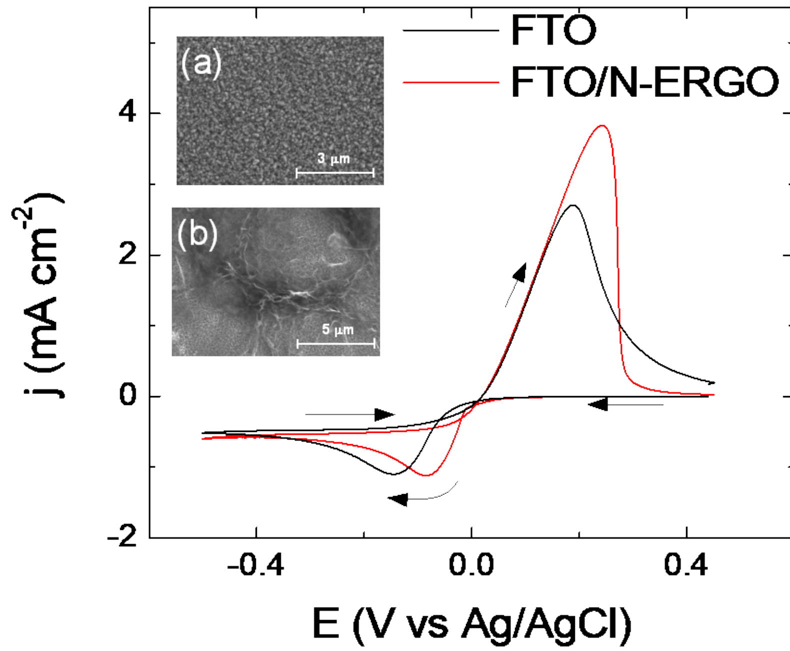

Figure 1: The voltammetric response of the FTO (black line) and FTO/N-ERGO (red line) electrodes in a 0.01 M $CuSO_4$ acidic solution (pH 1.00). In both cases, the scan rate was 10 mV s^{-1}. Insets show surface FESEM images of the FTO (a) and FTO/N-ERGO (b) electrodes before the cyclic voltammetry test.

FIGURE 2

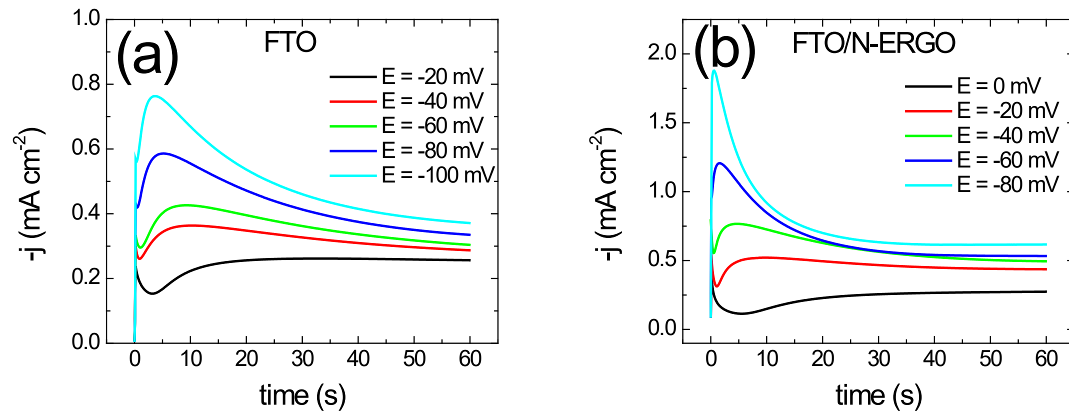

Figure 2: (a) Chronoamperometric curves (current transients j vs. t) of the FTO electrode in a 0.01 M $CuSO_4$ acidic solution (pH 1.00) at different potentials; (b) Chronoamperometric curves (current transients j vs. t) of the FTO/N-ERGO electrode in a 0.01 M $CuSO_4$ acidic solution (pH 1.00) at different potentials.

FIGURE 3

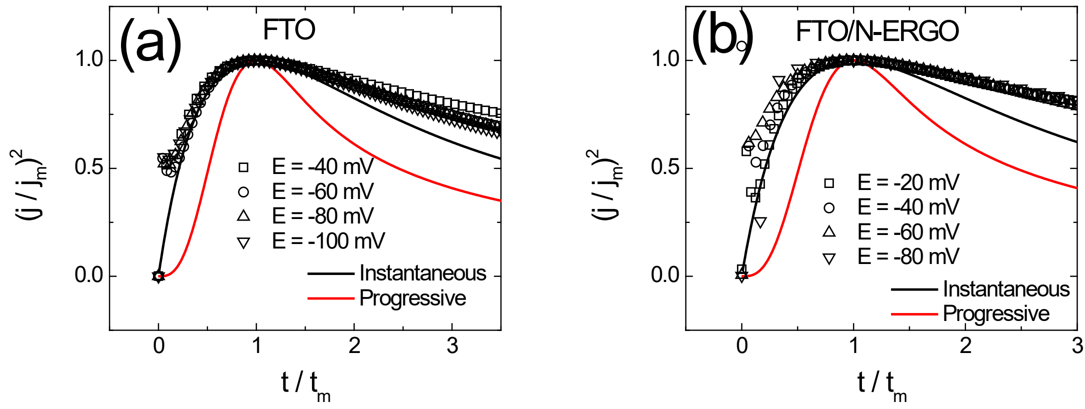

Figure 3: (a) Dimensionless plots $(j / j_m)^2$ vs. (t / t_m) for copper electrodeposition at different potentials onto FTO; (b) FTO/N-ERGO electrodes. Theoretical curves for IN-3D nucleation (equation (1), black line) and PG-3D nucleation (equation (2), red line) are also shown.

FIGURE 4

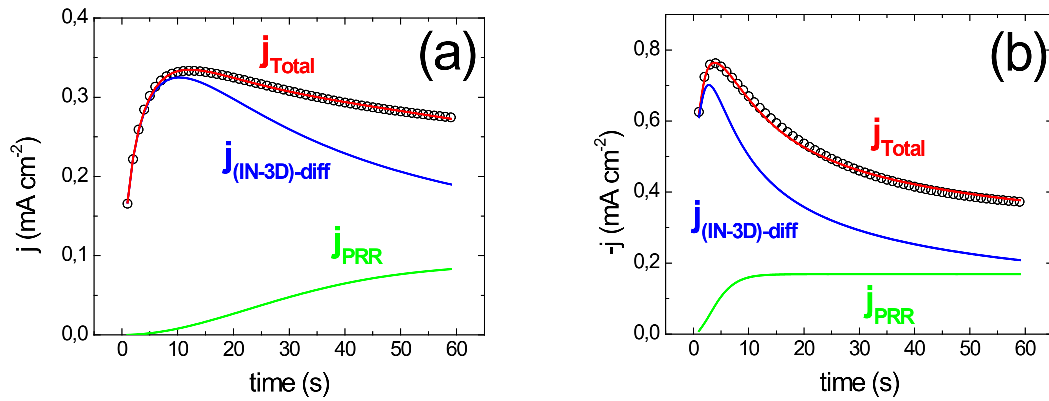

Figure 4: Current transient deconvolutions for copper electrodeposition (0.01 M $CuSO_4$, pH 1.00) onto FTO electrodes at –40 mV (a) and –100 mV (b). In both cases, the circles are the experimental curves and the continuous lines are the fitting procedures carried out in equation (9): $j_{(IN-3D)-diff}$ (blue line), j_{PRR} (green line) and j_{Total} (red line).

FIGURE 5

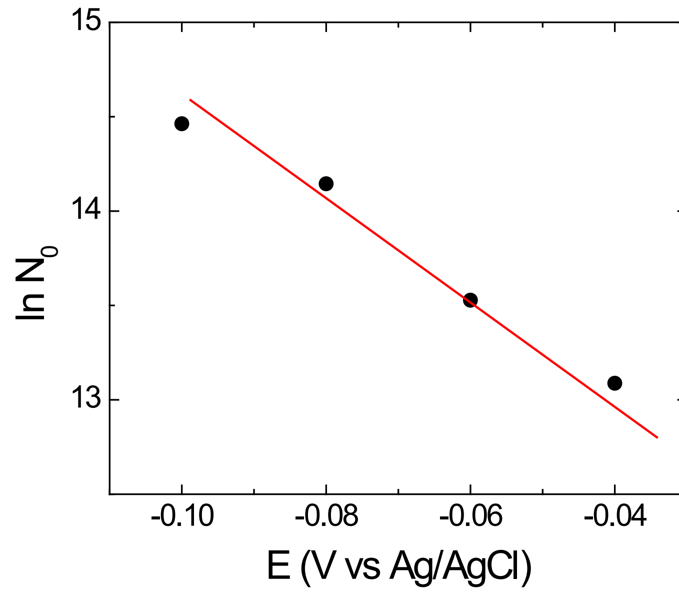

Figure 5: Dependence of the number of active sites per unit area (N_0) on the electrodeposition potential (semilogarithmic scale) for copper electrodeposition onto the FTO electrodes.

FIGURE 6

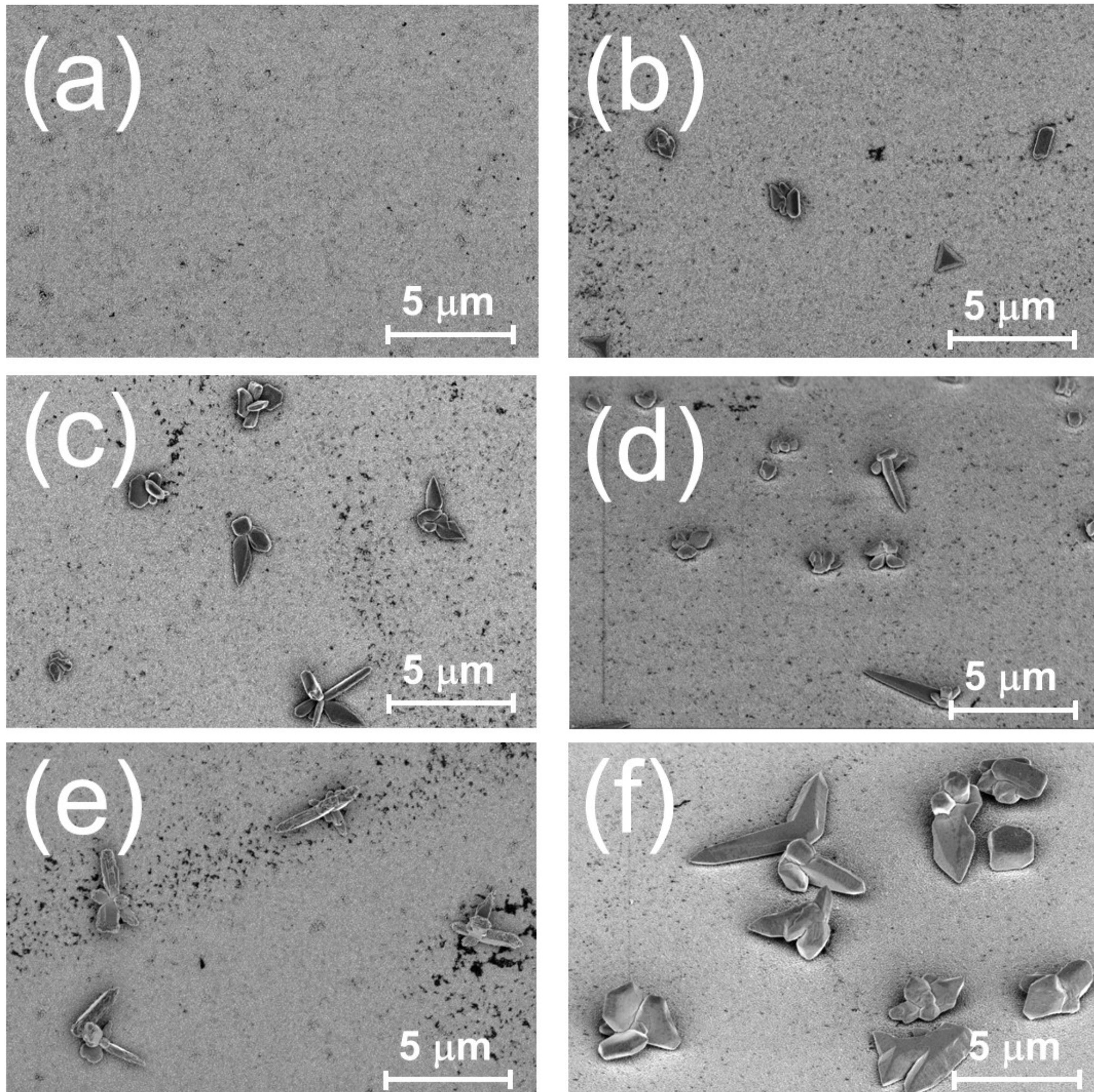

Figure 6: FESEM images of copper electrodeposits onto the FTO electrodes at different potentials: a) FTO substrate before copper electrodeposition; Copper electrodeposits at b) –20 mV, c) –40 mV, d) –60 mV, e) –80 mV and f) –100 mV. In all cases, the electrodeposition time was 60 s.

FIGURE 7

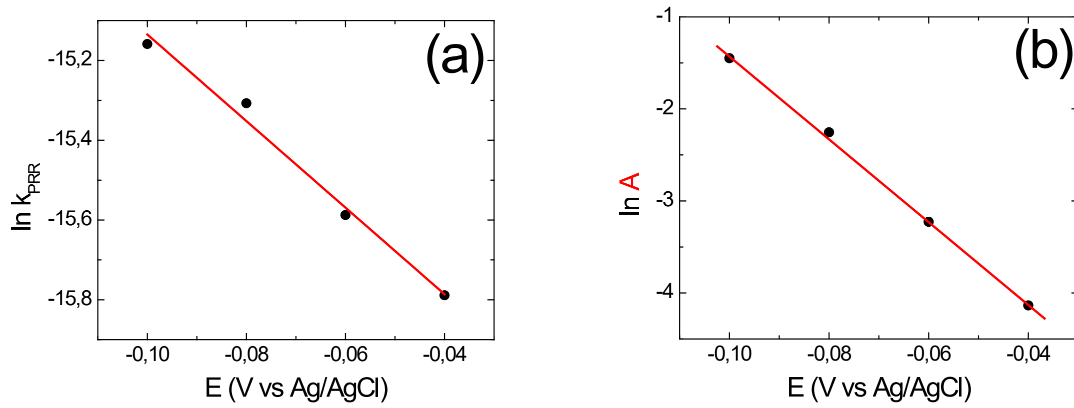

Figure 7: (a) Dependence of the kinetic constant for the proton reduction reaction (k_{PRR}), and (b) the nucleation rate per active site (A) with the copper electrodeposition potential (semilogarithmic scale) of copper electrodeposition onto the FTO electrodes.

FIGURE 8

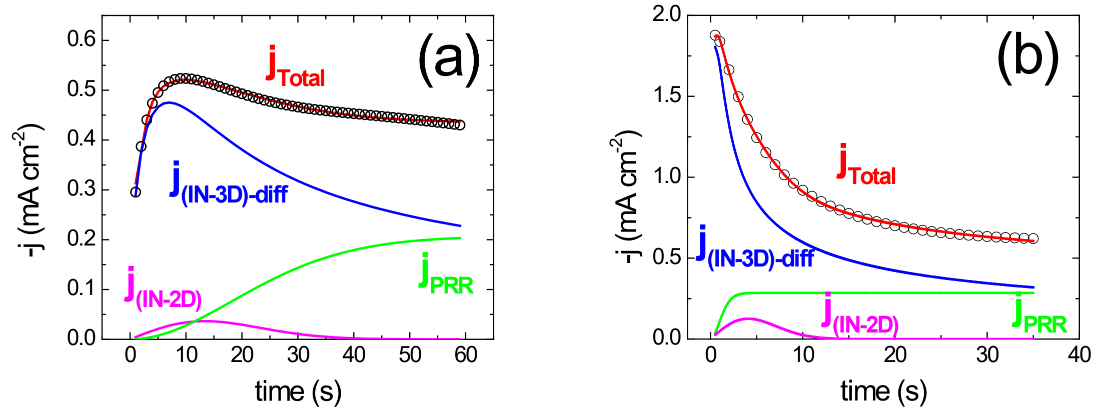

Figure 8: Current transient deconvolutions of copper electrodeposition (0.01 M $CuSO_4$, pH 1.00) onto the FTO/N-ERGO electrodes at –20 mV (a) and –80 mV (b). In both cases, the circles are the experimental curves and the continuous curves are the fitting procedures carried out in equation (16): $j_{(IN-3D)-diff}$ (blue line), j_{PRR} (green line), $j_{(IN-2D)}$ (purple line) and j_{Total} (red line).

FIGURE 9

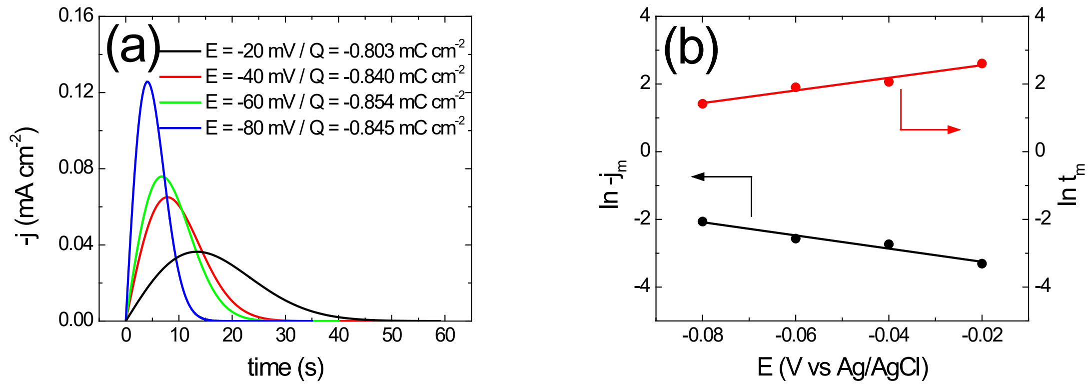

Figure 9: (a) Current vs. time transients of the IN-2D processes for copper electrodeposition onto the FTO/N-ERGO electrodes obtained through deconvolution of the curves in Figure 2 (b) using equation (16), and the electric charges (Q) involved in each of them. (b) Dependence of j_m (black dot) and t_m (red dots) on the potential in a semilogarithmic scale.

FIGURE 10

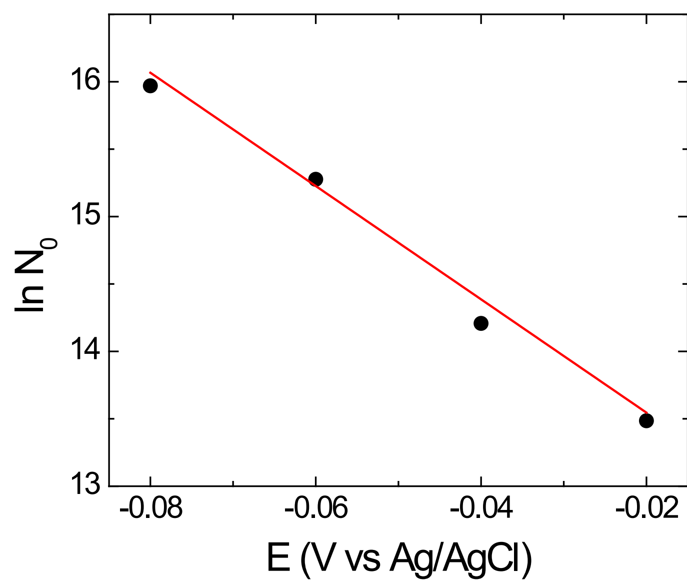

Figure 10: Dependence of the number of active sites per unit area (N_0) on the electrodeposition potential (semilogarithmic scale) for copper electrodeposition onto the FTO/N-ERGO electrodes.

FIGURE 11

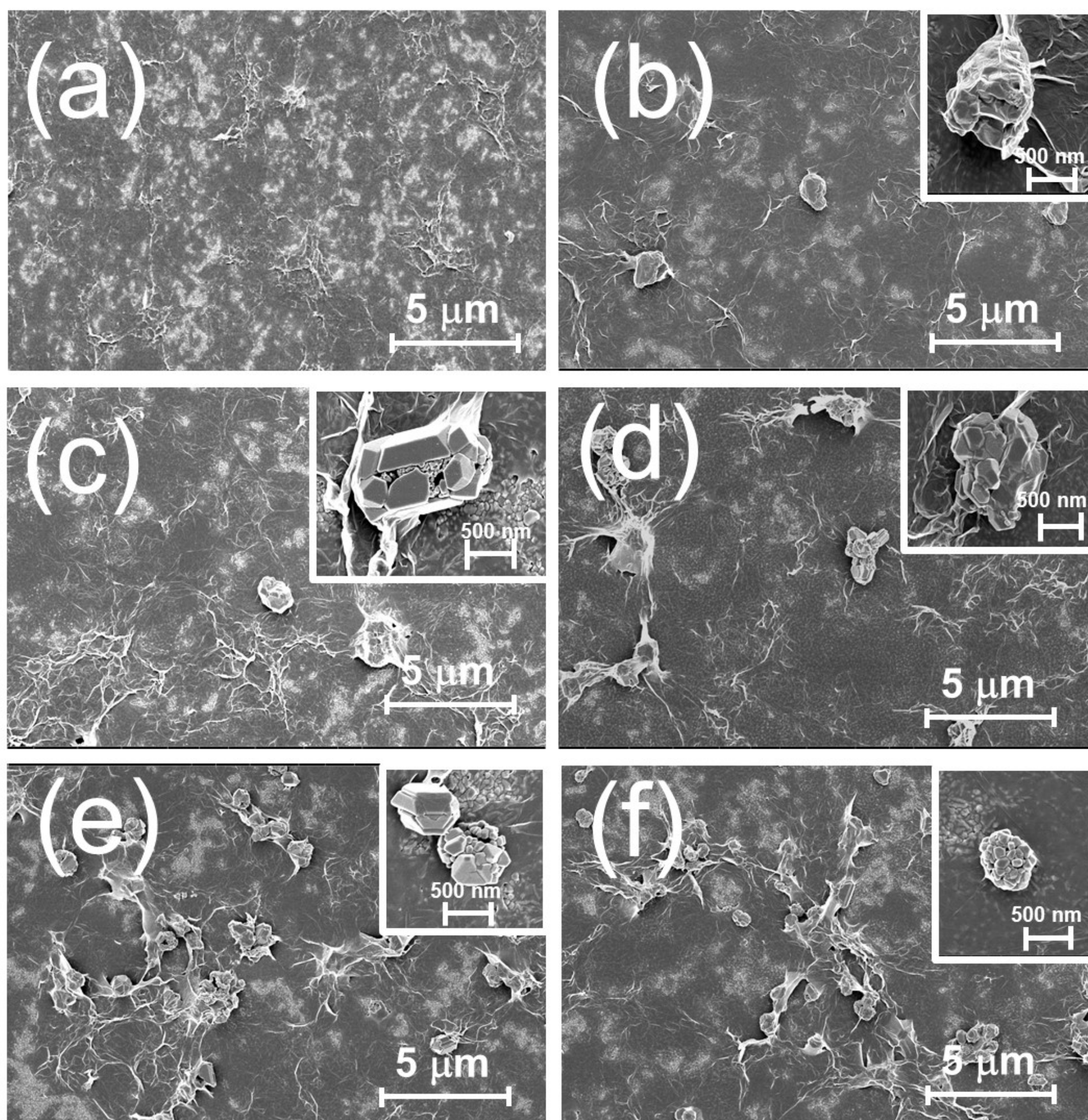

Figure 11: FESEM images of copper electrodeposits onto the FTO/N-ERGO electrodes at different potentials: (a) FTO/N-ERGO substrate before copper electrodeposition; Copper electrodeposits obtained at (b) 0 mV, (c) –20 mV, (d) –40 mV, (e) –60 mV and (f) –80 mV. In all cases, the electrodeposition time was 60 s.

FIGURE 12

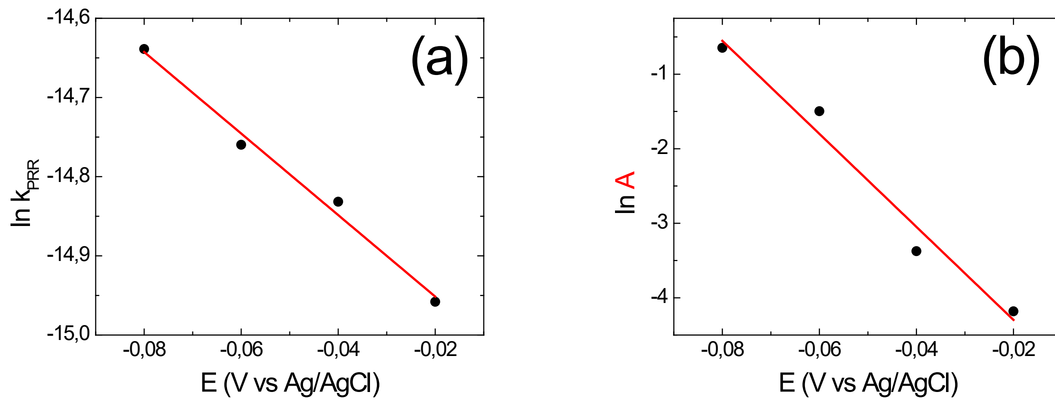

Figure 12: (a) Dependence of the kinetic constant for the proton reduction reaction (k_{PRR}), and (b) the nucleation rate per active site (A) with the copper electrodeposition potential (semilogarithmic scale) of copper electrodeposition onto the FTO/N-ERGO electrodes.